Eur. Phys. J. A (2026) 62:174
https://doi.org/10.1140/epja/s10050-026-01936-y

THE EUROPEAN PHYSICAL JOURNAL A

Regular Article - Experimental Physics

A new heavy ion tracking detector for the R^{3}B setup based on scintillating fibers and SiPM readout

P. Garcia Gil[1,2,3,a], I. Brandherm[4], M. Heil[1], D. Savran[1], C. Caesar[1], T. Aumann[1,2], E. Casarejos[3], J. A. Galvis Tarquino[1], H. Heggen[1], N. Kurz[1], D. Körper[1], C. Nociforo[1], C. J. Schmidt[1], H. Simon[1], S. Utz[1], R. Visinka[1], M. Winkler[1], A. Zilges[4]

[1] GSI Helmholtzzentrum für Schwerionenforschung, Planckstraße 1, 64291 Darmstadt, Germany
[2] Technische Universität Darmstadt, Fachbereich Physik, Institut für Kernphysik, 64289 Darmstadt, Germany
[3] CINTECX, Universidade de Vigo, DSN, Dpt. Mech. Engineering, 36310 Vigo, Spain
[4] Institut für Kernphysik, Universität zu Köln, 50937 Köln, Germany

Received: 16 April 2026 / Accepted: 15 July 2026
© The Author(s) 2026
Communicated by Piotr Salabura

Abstract We present the design, developments, and test results of the new scintillating fiber based tracking detectors which are part of the R^{3}B experimental setup at GSI and FAIR, Darmstadt, Germany. Those tracking detectors are capable to track heavy ions of all charges at relativistic energies. Together with an elaborate particle-tracking system, the full identification of relativistic ions from hydrogen up to uranium in mass and nuclear charge is possible.

1 Introduction

Tracking of heavy ions and reaction products is a core requirement for experiments with relativistic radioactive beams in inverse kinematics, as pursued within the NUSTAR research program at FAIR [1]. In particular, the reconstruction of particle trajectories through large-acceptance magnetic spectrometers relies on precise position measurements at several locations along the beam line. These measurements provide access to the magnetic rigidity and, in combination with time-of-flight and charge information, enable event-by-event particle identification and momentum reconstruction, which are essential ingredients of many experimental observables addressed by the R^{3}B experimental setup, for details on the setup we refer to [2].

Future experiments at FAIR place stringent demands on tracking detectors, combining high detection efficiency and good spatial resolution with the requirement of an extremely low and homogeneous material budget. The latter is of particular importance for heavy ions at relativistic energies, where energy-loss straggling and multiple scattering directly affect the achievable mass and momentum resolution [3]. At the same time, tracking devices must be compatible with operation inside magnetic fields and capable of handling the high beam intensities foreseen at FAIR.

Scintillating fiber–based tracking detectors have emerged as a well-suited solution to meet these requirements [4–7]. The Scintillating Fiber (SciFi) technology allows the realization of large-area detectors with single-particle tracking capability, fast timing signals, and high geometrical flexibility, while maintaining a low material budget and a scalable, cost-effective design. When combined with silicon photomultiplier readout [8], such detectors are insensitive to magnetic fields, enable compact detector layouts with a large number of readout channels, and allow stable operation without high-voltage systems.

In this paper, we present the development and characterization of a large-area scintillating fiber tracking detector intended for heavy-ion measurements in the R^{3}B setup at FAIR. The detector is optimized for precise position measurements along the ion flight path while minimizing the impact on the particle trajectories. Its performance has been investigated with particular emphasis on efficiency, spatial resolution, and suitability for operation under realistic R^{3}B experimental conditions.

2 Design goals

The primary design objective of the new tracking detector is the realization of an extremely low and homogeneous material budget in order to minimize angular and energy straggling of heavy ions. This requirement is particularly critical

[a] e-mail: pablo.garcia.gil@uvigo.es (corresponding author)

Published online: 14 August 2026

as the detector constitutes the first position-sensitive tracking device located downstream of the magnetic field. Any degradation of the ion trajectories at this stage directly impacts the precision of the momentum reconstruction and, consequently, the overall performance of the spectrometer.

Accurate position measurements behind the magnet are essential for determining the magnetic rigidity with high precision. In combination with the downstream time-of-flight measurement provided by the ToFD wall [9], this enables an unambiguous event-by-event determination of the mass and nuclear charge, even for heavy and exotic isotopes produced at FAIR. Minimizing straggling effects in the tracking detector is therefore a key prerequisite to fully exploit the resolution of the R^3B magnetic spectrometer and the ToFD system.

To meet these requirements, scintillating fibers with a square cross section of 0.2 mm $\times$ 0.2 mm are employed (Kuraray SCSF-78, 0.2mmSQ BSJ) [10], representing the thinnest commercially available fibers suitable for large-area detector construction. The fibers are arranged side by side to form a homogeneous scintillating ribbon, ensuring uniform response across the active area while keeping the amount of material traversed by the ions to a minimum. The detector is designed to cover an active area of approximately 50 cm $\times$ 50 cm, matching the large acceptance required for R^3B experiments.

Given the proximity of the detector to the magnetic field region, silicon photomultipliers are used as photosensors. Their insensitivity to magnetic fields, compact form factor, and compatibility with a large number of readout channels make them well suited for operation in the R^3B environment. The chosen design thus optimally balances tracking performance, material budget constraints, and experimental integration requirements.

3 Scintillating fiber ribbon production

The scintillating fiber ribbon is produced using a dedicated winding machine located at the GSI detector laboratory. Originally developed for the winding of wires, this infrastructure has been upgraded in recent years to allow the controlled production of fiber ribbons. The machine is designed to fabricate single-layer ribbons based on scintillating fibers with a square cross section and provides precise control and monitoring of the applied fiber tension during the winding process. Comparable concepts have been employed in other large-scale experiments, such as the LHCb Scintillating Fibre Tracker [11]; however, in that case the winding procedure was limited to fibers with circular cross sections.

During production, the fibers are wound onto the winding body with the minimum achievable tension in order to reduce mechanical stress. For square fibers of comparable size, a tension of approximately 0.02 N has been found to be sufficient to ensure stable handling while avoiding damage to the fibers. Throughout the winding process, the individual fibers are continuously pressed against each other, resulting in a dense, gap-free ribbon structure. This approach ensures that variations in the individual fiber widths do not translate into gaps within the ribbon and eliminates the need for a predefined pitch, which would inevitably introduce non-active regions.

The gap-free winding procedure offers several advantages. It minimizes the fraction of non-active material, avoids glue between adjacent fibers, and prevents adhesion between the ribbon and the winding body. As a result, the ribbon can be removed from the winding body without mechanical stress. Moreover, this production method guarantees a highly homogeneous material distribution across the active area, which is essential for preserving the quality of the tracking information.

As winding body, a cylindrical aluminum drum with a diameter of 50 cm and a length of 80 cm is used. This geometry allows the production of continuous fiber ribbons of sufficient size to cover the required active area in a single piece. Once the winding is completed, a thin black light-tight foil with a thickness of 10 μm is glued onto the exposed fiber surface using epoxy adhesive (Epo-Tek 301-2), covering the full area of the ribbon.

In a subsequent step, the ribbon is cut at a single position in a direction perpendicular to the fiber orientation, allowing it to be removed from the cylindrical winding body. The ribbon is then transferred onto a flat surface, where a second black light-tight foil is glued to the opposite side. This final step ensures full light tightness and provides additional mechanical stability. After curing, the ribbon remains flat and mechanically robust, and is ready to be integrated into the mechanical support structure described in the following section. The total thickness of the produced ribbon is measured at different positions using a micrometer screw gauge to be 0.24 m with a variation of less than 0.01 μm.

3.1 Quality control

The quality of the produced scintillating fiber ribbons was evaluated by means of optical inspection using a microscope. Since the fiber ribbon was produced longer than required for detector assembly, dedicated samples could be prepared for quality control without affecting the active detector area. A section of the ribbon was fixed between two plastic plates, after which the ends were precision-milled. This ensured that the fiber ends and the plastic plates formed a smooth and flat surface suitable for high-quality microscopic inspection.

Figure 1 shows a microscopic image of the cross section of a section of the fiber mat, allowing a direct assessment of the fiber geometry, packing density, and uniformity. For imag-

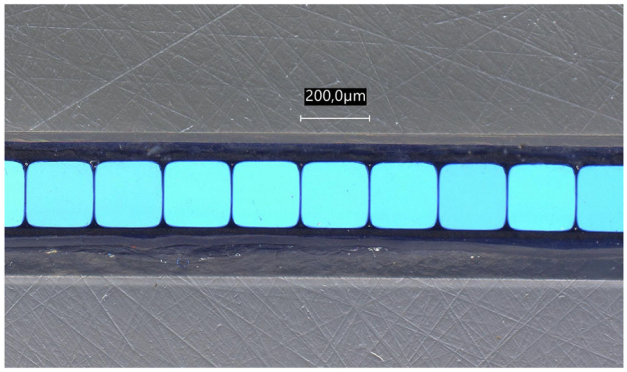


Fig. 1 Microscopic image of the cross section of a section of the scintillating fiber ribbon used for quality control. The fibers are illuminated from the rear side, clearly resolving the square fiber geometry and demonstrating the uniform, gap-free packing achieved during the winding process. The dark regions between the blue fiber cores correspond to the cladding of the fibers. No gaps in between neighboring fibers are observed

ing, the fibers were illuminated from the rear side, providing high contrast and clearly resolving the square cross section of each fiber. The full microscope scan covers a 10 cm wide section of the ribbon, which corresponds to the maximum width achievable with the stitching capabilities of the microscope system. For clarity, only a representative subsection of this scan is shown in the figure.

The complete stitched microscope image was analyzed, and the distances between the edges of neighboring fiber was extracted, corresponding to the fiber width including the cladding. The resulting distribution is shown as a histogram in Fig. 10 (orange histogram). From this analysis, an average fiber width of $d = (190.77 \pm 0.07)\mu m$ was determined, with a standard deviation of $\sigma = (1.52 \pm 0.07)\mu m$. The measured mean width is slightly smaller than the nominal value of 200 μm, but remains fully within the specifications provided by the manufacturer (Kuraray). The observed width variation is below 1%, demonstrating the high production stability and uniformity of the scintillating fibers. These results confirm the geometrical quality of the ribbon and the suitability of the production process for detectors requiring a highly homogeneous and well-controlled material distribution.

4 Readout electronics

The scintillation light is read out at both ends of each fiber using Hamamatsu S13552 Multi-Pixel Photon Counter (MPPC) arrays [12]. Compared to conventional photomultiplier tubes, SiPMs offer several advantages, including compactness, operation without high voltage, and a lower cost per channel. For the present application, the most relevant features are their one-dimensional array geometry and insensitivity to magnetic fields.

The S13552 is a one-dimensional 128-channel SiPM array with a spectral sensitivity well matched to the emission wavelength of the scintillating fibers. Each channel has a pitch of 0.25 mm and a height of 1.6 mm. While the pitch is slightly larger than the fiber width of 0.2 mm this mismatch is mitigated by the lateral spread of scintillation light across multiple channels. As will be discussed in the analysis section, this allows for a reliable reconstruction of the fiber position despite the non-matching pitch.

The SiPM arrays are mounted in a single row on a custom PCB (SciFi_FEB512) and positioned as close as possible to the PCB edge. Each PCB hosts four S13552 arrays, arranged with minimal spacing and reduced inactive margins at the edges, enabling an almost gap-free tiling of adjacent boards. This results in a photosensor assembly that closely matches the form factor of the fiber ribbon.

The analog signals from the SiPMs are processed by MPPC_ROB3 readout modules developed by the GSI Electronics Department [13]. Each module provides 128 channels with discrete, very low-power preamplifiers (gain G $\approx$ 25–30). The preamplifiers have been designed using air coils to allow operation close to magnetic fields. For each channel, an individual discriminator threshold can be set, allowing for a flexible adjustment to channel-to-channel variations. The signals are digitized by measuring the leading and trailing edges with an FPGA-based TDC with a resolution of approximately 170 ps RMS, corresponding to the times at which the signal crosses the discriminator threshold. From these measurements, the time-over-threshold (ToT) is determined for each signal, providing a measure of the signal amplitude and thus the amount of detected scintillation light.

The modules can accept and generate trigger signals. The TDC data are transmitted via a 5 Gbps optical serial interface. The readout boards incorporate Hamamatsu C14156 boost converters, which generate the required SiPM bias voltage ($>$ 50 V) locally from a 5 V supply. The total power consumption per board is 12 W (12 V, 1 A), corresponding to approximately 90 mW per channel.

Operation of the readout system in vacuum requires active water cooling. Two independent cooling circuits are implemented. The first circuit operates at approximately 20 °C and is dedicated to the readout electronics, in particular the FPGA, where the majority of the power dissipation occurs and cooling is required primarily to maintain a stable operating temperature. The second circuit cools the SiPM arrays. While MPPCs are commonly cooled to reduce the dark count rate (e.g., the LHCb experiment operates the same device at -40 °C [6]), the high photon yields in this system leads to an envisaged stable, operating temperature of approximately 10 °C. In this case, only negligible power is dissipated, and the cooling system is optimized to provide a low and highly stable temperature in order to minimize noise. Four readout

boards together with their associated cooling elements form a single readout block, as shown in the 3D model, see Fig. 3.

5 Mechanical design

This section describes the mechanical design of the new detector, including the design requirements, the main support structure, the integration of the scintillating fiber ribbon, and the implementation of the readout electronics and cooling systems.

5.1 Design requirements

The mechanical design of the detector was driven by the following requirements:

- Integration inside the R^3B main vacuum chamber, with the detector center aligned to the beam height and sufficient clearance for the horizontal drive system located underneath.
- An active area of at least $50 \times 50\ cm^2$.
- Minimal material budget on the side facing the neutron branch in order to suppress background from secondary interactions.
- Mechanical stability sufficient to preserve the alignment of the scintillating fiber ribbons and maintain the intrinsic position resolution.
- Implementation of two independent cooling circuits, as required by the readout electronics and SiPM operating conditions (see Sect. 4).

The active width of the detector is defined by the granularity of the SiPM arrays and the corresponding PCB layout (integer multiples of its width). The active height is mainly constrained by the available space inside the vacuum chamber, the attenuation losses in the scintillating fibers is only of minor importance here.

In order to ensure that structural deformations do not significantly affect the spatial resolution, the mechanical deformation of the structure must be carefully controlled. In the horizontal direction (perpendicular to the fiber orientation), the maximum allowed deformation is limited to twice the fiber width (400 μm), ensuring that any residual misalignment can be corrected using the alignment system of the top plate. In the vertical direction (along the fibers), a maximum deformation of three times the fiber width (600 μm) is permitted to prevent uneven mechanical tension in the ribbons and to guarantee the proper operation of the tensioning system.

5.2 Structure main frame

The resulting detector provides an active area of approximately 50 cm in width and 60 cm in height. The increased height, enabled by the compact readout electronics, offers additional flexibility for experimental configurations while remaining compatible with the available installation space.

The main frame consists of two C-shaped aluminum structures connected to each other to provide the required rigidity. This geometry leaves the side between the neutron and heavy-fragment branches largely free of material, thereby minimizing additional background contributions. The majority of structural components are manufactured from aluminum alloy AW-5051, while selected small parts are made from stainless steel AISI-304. Both materials are vacuum compatible and suitable for operation in the vicinity of magnetic fields.

The mechanical stability of the structure was evaluated using finite element method (FEM) simulations. An iterative optimization process was performed to minimize deformations under the worst-case load conditions considered in the design. The final deformation map is shown in Fig. 2. In addition, a removable stiffening arm can be installed to close the open side of the C-frame structure when increased rigidity is required.

5.3 Fiber ribbon support and alignment

The scintillating fiber ribbon is clamped and glued at both ends by aluminum fixtures mounted to the top and bottom plates. This design allows replacement of the ribbon in case of radiation damage. The plates define the relative position between the ribbon and the SiPM arrays and mechanically connect the two main frame elements.

The distance between the fiber ribbon and the SiPM arrays is defined by the plate geometry to ensure efficient optical coupling. Due to the 0.2 mm fiber diameter and the 1.6 mm SiPM channel height, a finite separation is required to illuminate the full SiPM cell area. For the present design, a gap width of 1 mm between the end of the fibers and the SiPMs is selected. The gap is filled with optical coupling material (QSil 217) during assembly.

To maintain uniform tension in the ribbon, the bottom plate is spring-loaded. The spring force is adjustable and selected such that the fiber stress remains safely below the yield strength of the material. The top plate is fixed vertically but allows horizontal adjustment to compensate for residual misalignments between top and bottom supports.

5.4 Electronics integration

The readout electronics are mounted at both ends of the fiber ribbon on the top and bottom plates. The readout PCBs

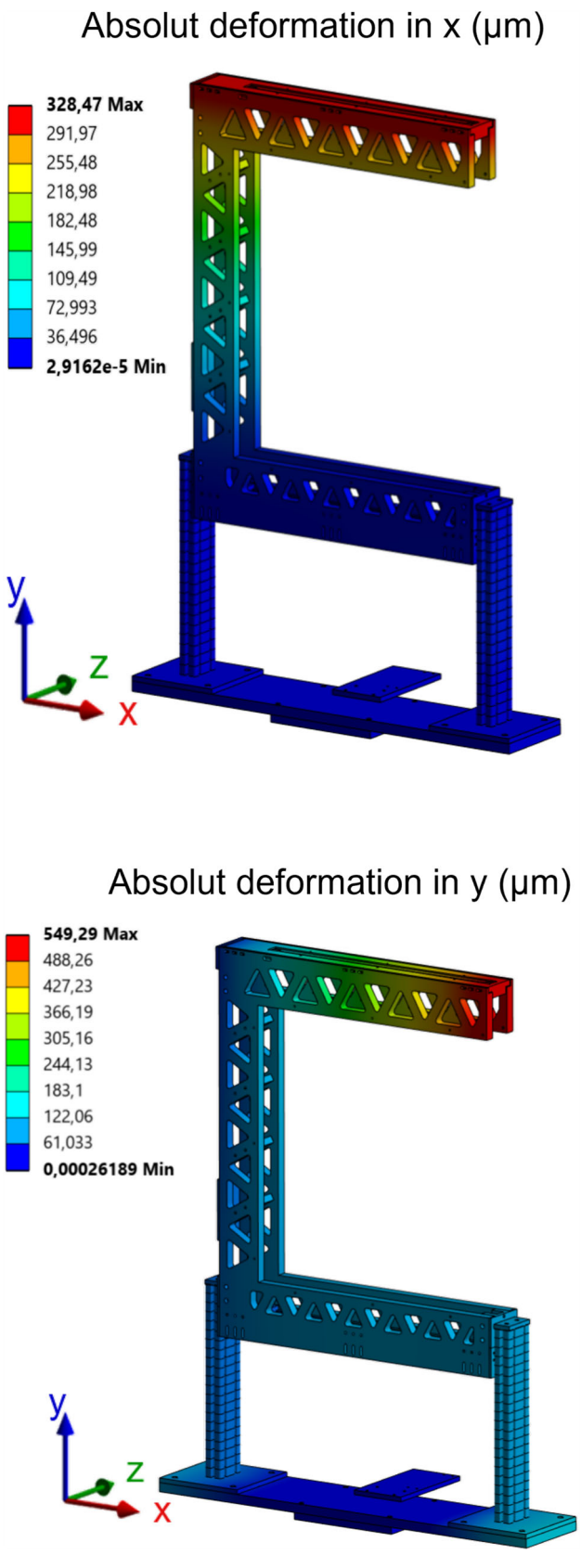


Fig. 2 FEM analysis of the detector structure

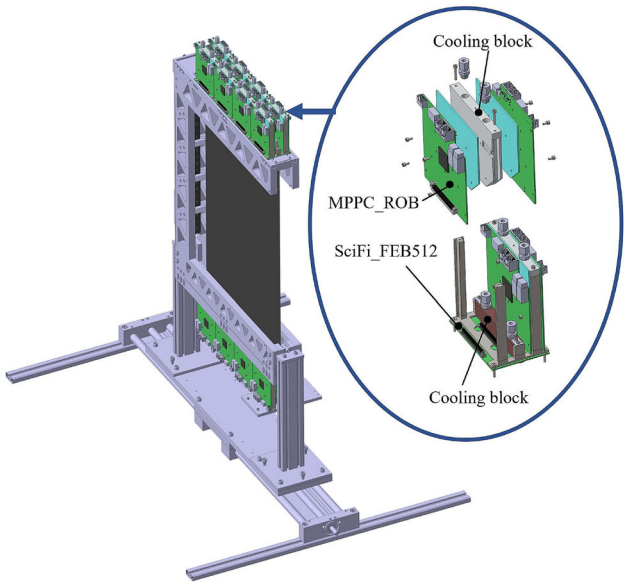


Fig. 3 3D model of the fully assembled detector

(MPPC_ROB3, see Sect. 4) are mechanically supported via the cooling structures.

Two types of water-cooled bodies are implemented. The first type, manufactured from aluminum, is designed to dissipate the heat generated by the FPGA boards. Each cooling block serves two FPGA boards mounted on opposite sides with thermal interface material in between. The second type, made of oxygen-free copper, cools the SiPM arrays located on the rear side of the PCB.

The two cooling systems operate as independent circuits with different operating temperatures and flow rates, optimized for their respective thermal loads, as described in Sect. 4. Thermal tests under both air and vacuum conditions confirmed stable and efficient operation.

A fully assembled view of the detector and a detailed representation of the cooling integration are shown in Fig. 3. There one sees four SciFi_FEB512 PCBs mounted in one row on top and bottom respectively, yielding a total number of 4k ($4 \times 4 \times 128 \times 2 = 4096$) readout channels.

6 Commissioning of the final detector

The performance of the completed scintillating fiber tracking detector, hereafter referred to as Fib70, was investigated during a beam time behind the GLAD dipole magnet [14] within the R^3B experimental setup. The beam time was dedicated to detector commissioning, during which several detectors were installed sequentially along the beam line to maximize the efficient use of the available beam. As primary beam, ^{107}Ag ions with an energy of 1 GeV/u were delivered to the

experimental area, with typical intensities between 10 and 100 kHz.

In addition to Fib70, a second scintillating fiber detector, denoted Fib41, was operated during the same beam time. Fib41 was positioned approximately 30 cm downstream of Fib70 and consists of scintillating fibers with a square cross section of 500 μm, read out by a multi-anode photomultiplier tube. In this detector, each fiber is directly coupled to one readout channel, resulting in a trivial and unambiguous position determination for traversing ions. A detailed description of the Fib41 detector will be presented elsewhere. Due to its straightforward position reconstruction, Fib41 was used as an external reference detector for position measurements and for the characterization of the performance of Fib70.

Both detectors were mounted on precision linear translation stages, allowing movement perpendicular to the incident beam direction. The coordinate system is defined such that the x-axis is horizontal and perpendicular to the beam, the y-axis is vertical and perpendicular to the beam, and the z-axis coincides with the beam direction and is perpendicular to the fiber plane. The scintillating fibers in both detectors were aligned parallel to the y-axis, providing position information along the x-coordinate. The linear stages allowed the detectors to be scanned along the x-axis, such that for a fixed beam position centered on the detector, all fibers could be individually probed. In addition, this setup allowed for controlled variations in the relative position between Fib70 and Fib41.

6.1 Data analysis

In the following, two complementary data sets are analyzed to characterize the detector performance. The first data set corresponds to a so-called sweep run of Fib70, in which the detector was repeatedly moved along the x-axis using the linear translation stage. By scanning the detector position across the ^{107}Ag beam, the full width of Fib70 was exposed to the beam, ensuring that each fiber was hit by ions a sufficient number of times. This data set allows a systematic investigation of the response and performance of all fibers across the detector. The second data set was recorded with both Fib70 and Fib41 kept in fixed positions. In this configuration, Fib41 provides a stable external position reference for the ions traversing Fib70 enabling a detailed characterization of the position response, efficiency, and resolution of Fib70. The analysis procedures applied to these two data sets are described in the following sections.

6.1.1 Time-over-thresholds

The light generated by an ion interacting with the scintillating fibers is quantified using a time-over-threshold (ToT) technique applied to the measured signals from the SiPM channels. As described above, the ToT provides a measure of the signal amplitude and thus of the detected scintillation light.

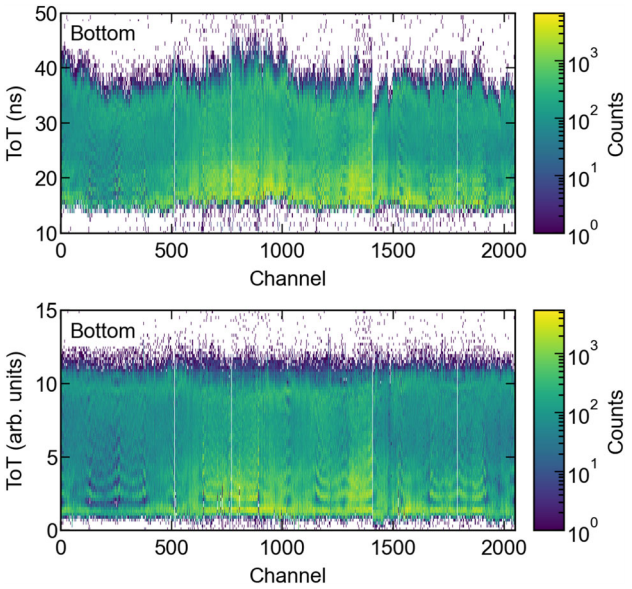


Fig. 4 (top) Time-over-threshold spectrum of the bottom side of the Fib70 detector. (bottom) The same time-over-threshold spectrum in (arb. units) after correcting the SiPM channels with regard to their different gains

The ToT response of the Fib70 detector was evaluated using the sweep run introduced in Sec. 6.1, in which the detector was moved horizontally through the ^{107}Ag beam to achieve a illumination along the x-axis. The resulting ToT spectrum for the bottom side of the detector is presented in Fig. 4 (top). During this measurement, the typical ToT of events ranged from 15 ns to 45 ns.

Figure 5 shows the ToT distributions of two channels from the same SiPM chip. The top panel shows channel 992 of the bottom detector, located at the centre of a SiPM chip. The lower panel shows channel 1024, which is the outermost channel on the same chip. Variations in the ToT between SiPM channels are caused by differences in their gain as well as the fact, that single fibers are not matched to individual SiPM channels.

In the ToT spectra of individual channels, peak-like structures can be observed, which are more pronounced for some channels than for others, as illustrated in Fig. 5. These structures do not correspond to the discrete photon peaks sometimes observed in SiPM signals associated with a defined number of detected photons, which has been verified in tests with UV generated scintillation light. However, the same tests verified the principle correspondence of the measured ToT to the total amount of light on a channel and that the peak structures represent only a local modification. The origin of these features remains unclear and is tentatively attributed to effects within the readout electronics. As they do not affect the subsequent analysis, they are not further investigated.

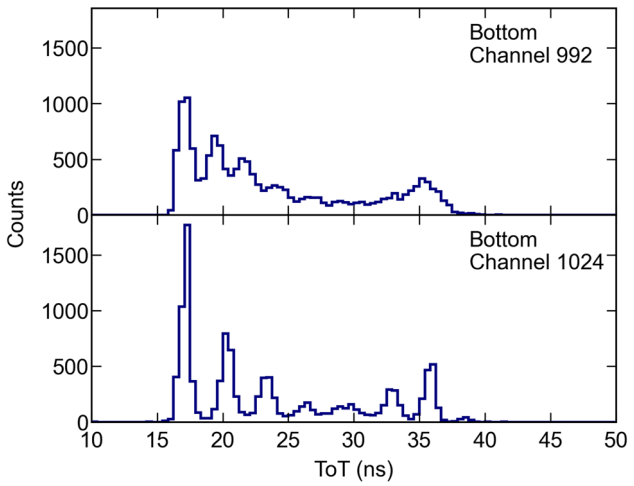


Fig. 5 (top) ToT distribution for channel 992 of the Fib70 detector detector. This readout channel is located in the center of a SiPM chip. (bottom) Same for readout channel 1024, which is located at the edge of a SiPM chip

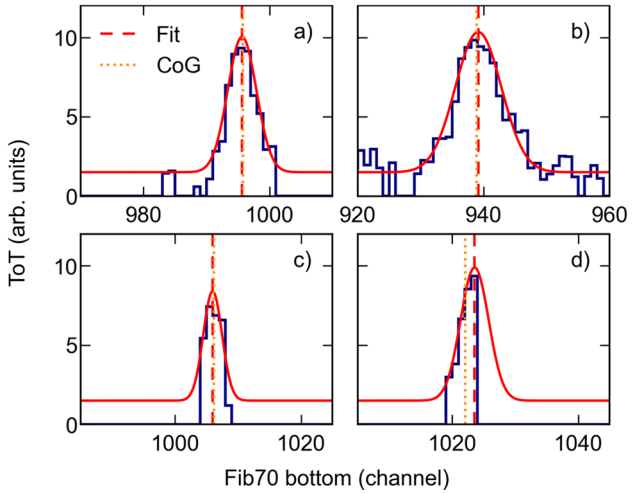


Fig. 6 Examples of ToT distributions of events recorded in the Fib70 bottom detector. The reconstructed positions obtained with the fit and CoG methods are shown, as well as the fitted Gaussian. Further details on panels a)–d) can be found in the text

6.1.2 Gain match

To address gain variations, a linear calibration of the time-over-threshold (ToT) values is implemented for each channel, mapping the individual ToT response to a common scale. For each channel, the first t_f and last t_l turning points of the ToT distributions are determined by evaluating the zeros of the second discrete derivative, defining the dynamic range of the signal. The ToT value for the i-th channel, T^i, is converted using the following expression:

$$T^i_{gm} = a\left(T^i/g^i - t^i_f/g^i\right) + b, \tag{1}$$

with $g^i = t^i_l - t^i_f$. Here, g^i corresponds to the effective ToT range of the channel. A common offset b is used for all channels to shift the smallest ToTs to slightly positive values, while a normalization factor a is applied to scale the largest ToT to approximately 10. Due to channel-dependent scaling factors g_i, the ToT after gain matching is expressed in arbitrary units (a.u.) instead of nanoseconds. The ToT distribution after gain matching is shown in the bottom panel of Fig. 4 and shows a clear mitigation of previously visible fluctuations. In the following, the so calibrated ToT values are used to determine the position of interaction of a beam particle with the detector.

6.1.3 Position reconstruction

For each event, the signals from the two sides of the detector (top and bottom) are treated independently, and the position is reconstructed separately for each side. Due to the 1 mm gap between the fiber ribbon and the SiPM arrays, the scintillation light produced within a single fiber is distributed over several adjacent SiPM channels on both sides. This leads to the formation of clusters, defined as groups of adjacent SiPM channels that register light from the same event. The task of the position reconstruction is, therefore, to determine the interaction position from the measured ToT values of these channels. In the following, a gap of one channel within a cluster is allowed to account for malfunctioning readout channels. Examples of such ToT distributions are shown in Fig. 6. The distributions illustrate how the light from a single ion interaction is shared among multiple channels, forming a cluster whose shape reflects the underlying light distribution. This also demonstrates, that the peak like structures in the ToT spektra of individual channels (as explained above in Fig. 5) do not disturb the correlation of the measured ToT values to the amount of light detected by on SiPM channel.

In the following, only clusters with at least one channel exceeding a ToT of 7 a.u. are considered. This threshold effectively excludes background events. Figure 7 presents the distribution of cluster sizes for the bottom side of Fib70. In this measurement, the typical cluster size is about 13, with the distribution showing a tail towards very large clusters. The average cluster size is influenced by the experimental conditions, including the ion species and energy, which affect the light yield, as well as the bias voltages and thresholds applied to the SiPM readout.

The channel with the largest geometric overlap with the fiber that was hit by the ion typically records the highest ToT value within a cluster. The interaction point with the detector – which serves as the key observable for tracking – is therefore determined by reconstructing the center of the ToT distribution and, thus, identifying the fiber that was hit.

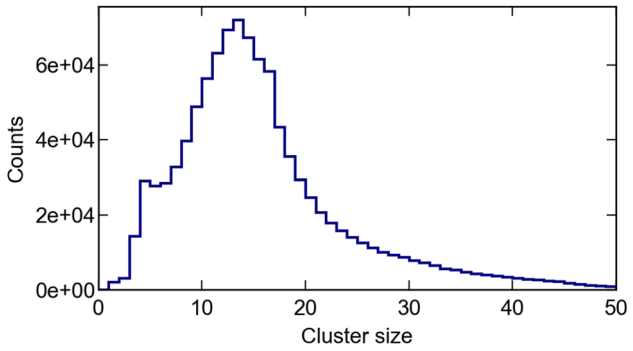


Fig. 7 Distribution of cluster sizes of the Fib70 bottom detector

In our analysis, we follow two approaches to determine the center of a cluster: the center of gravity (CoG) method and a Gaussian fit, both of which are discussed below.

In the centre-of-gravity method, the position of a hit x_g is determined by

$$x_g = \sum_i x_i T^i_{gm} / \sum_i T^i_{gm}, \tag{2}$$

where x_i denotes the i-th channel and T^i_{gm} the gain-matched ToT.

In the "Fit" method, a Gaussian of the shape

$$f(x) = \frac{A}{\sqrt{2\pi}\sigma} \exp\left(-\frac{1}{2}\left(\frac{x - x_f}{\sigma}\right)^2\right) + c, \tag{3}$$

is fitted to the ToT distributions of a single event. Thereby, σ denotes the standard deviation, A the amplitude, and c the offset. The centroid x_f gives the position of the cluster. For this method, a minimum cluster size of four is imposed to ensure a meaningful fit. Fits are accepted only if the amplitude and standard deviation parameters fall within reasonable ranges, and events exhibiting large reduced χ^2 values are excluded. These criteria ensure that only events that permit an unambiguous determination of the center of the ToT distribution are used, thereby achieving the highest possible accuracy in position determination. However, compared to the CoG method, these additional conditions result in a smaller number of reconstructed cluster positions and thus a reduction in efficiency.

The results of the two methods are also shown in Fig. 6. For the majority of events recorded in the experiment, the ToT distribution has an approximately Gaussian shape, as shown in panels a) and b). Deviations from this behavior appear mostly at the edges of the SiPM arrays. As examples, panel c) depicts an event with a smaller cluster size of 5, resulting in a less pronounced Gaussian shape. Panel d) shows the ToT distribution for an event occurring near the edge between two PCBs. The gap between the PCBs causes the cluster to terminate at channel 1024, resulting in the right-hand side of the light distribution not being recorded.

The fit and CoG methods yield identical centroids when the ToT distribution is perfectly Gaussian. For skewed or incomplete distributions, the resulting positions may differ, as shown in panel d) of Fig. 6, where the CoG result is lower than the fit result. The CoG method evaluates only the available information and does not impose assumptions on signal shape or distribution. In contrast, the fit method assumes a specific shape for the ToT distribution, which can compensate for incomplete data. However, if an event produces a non-Gaussian ToT distribution, the CoG method can still reconstruct a position, whereas such events are likely to be excluded from the fit analysis due to the additional conditions mentioned above. Furthermore, the fit method enables quality control of event reconstruction, which is not possible with the CoG method.

6.1.4 Mapping of channel number to position

The result of the procedures described above is the determination of the cluster centers (in units of channels) on both sides of the detector for each detected particle. For tracking heavy ions, the channel number of the Fib70 detector must be mapped to a position on the detection plane. Although the scintillating fiber ribbon itself is gapless, the SiPM readout is not, due to its 'PCB layout'. Three effects have to be considered.

First, the Hamamatsu S13552 SiPM array consists of two separate chips, each providing 64 readout channels. The distance between these chips is $d_{\text{chip}} = 220\,\mu$m [12]. Second, a gap exists between adjacent SiPM arrays soldered onto the same PCB. This distance can be measured directly by inspecting the PCBs with a microscope, yielding a mean gap size of $d_{\text{array}} = 570\,\mu$m. The third type is the gap between two neighboring PCBs, consisting of the distance from the edge of the last SiPM array to the edge of the PCB and the gap between the PCBs themselves. As the total width of this gap only becomes apparent after full detector assembly, it cannot be directly measured by visual inspection.

The size of the different gaps can be determined by analyzing the positional differences of correlated events recorded by the Fib41 and Fib70 detectors. As described above, Fib41 does not exhibit gaps in the readout due to its detector design and the one-to-one mapping of fibers to readout channels via a multi-anode photomultiplier. It therefore provides a reliable reference for the position measurement.

For each ion detected in both detectors, the interaction points x_{fib70} and x_{fib41} are determined. In a first step, the channel numbers of both detectors are converted into positions assuming a continuous, gap-free readout. This conversion is performed by multiplying the channel number by the respective channel pitch, which is $500\,\mu$m for the Fib41 detector

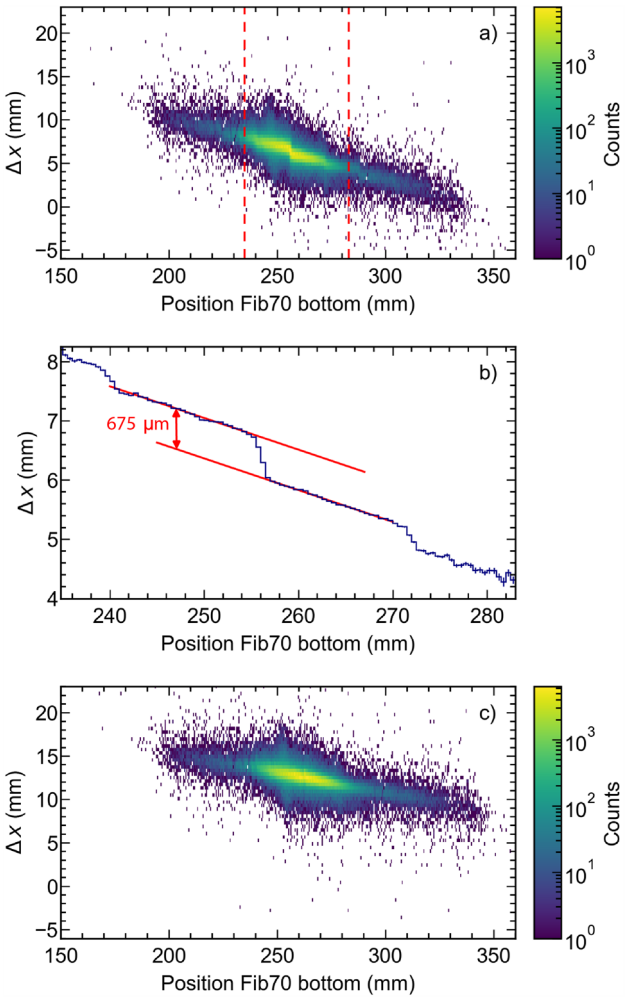


Fig. 8 **a** Position difference Δx of hits simultaneously recorded in the Fib41 and Fib70 bottom detector without correcting the position in Fib70 for the gaps between SiPM chips, SiPM arrays and PCBs. The expectation value in Δx of the area within the dashed red lines is shown in panel **b** together with piecewise linear fits of the steps. **c**) Same as panel a), but with corrected position of hits recorded with the Fib70 bottom detector

and 250 μm for the Fib70 detector. Under these assumptions, the event position difference, $\Delta x = x_{\text{fib70}} - x_{\text{fib41}}$, should remain constant if both detectors were perfectly aligned and free of gaps.

The position difference Δx is shown in Fig. 8 a) as a function of the hit position for the bottom side of Fib70. In this run, the beam was focused on the center of the Fib70 detector, directly covering the gap between the second and third PCBs. The distribution of Δx exhibits a global tilt as well as a clear discontinuity at a position of 260 mm. The tilt arises from a slight angular mismatch between the beam direction and the detector planes, combined with the finite distance between Fib41 and Fib70, resulting in a position-dependent offset between the two detectors. The discontinuity at 260 mm originates from the gap between the PCBs.

The expectation value of Δx from the region between the dashed red lines is shown in Fig. 8 b). In this representation, the discontinuities of Δx at the positions of the gaps in Fib70 become more evident. A stair-like pattern is observed, with each discrete step corresponding to a gap in the Fib70 bottom side. The steps at positions of 240 mm and 272 mm arise from gaps between chips of the SiPM arrays, while the larger step at 256 mm is due to the gap between the PCBs. By fitting these steps piecewise with linear functions, the gap sizes can be determined.

This results in 675 μm for the bottom side of the Fib70 detector and 668 μm for the top side. The average value of $d_{\text{pcb}} = 661\,\mu$m is adopted in the following for all gaps between PCBs.

With this information, the channel number of Fib70 can be converted into a corrected position on the detection plane by explicitly accounting for the gaps in the SiPM readout. Figure 8 c) shows the position difference Δx as in panel a), but now using the corrected positions for Fib70. In contrast to the initial conversion assuming a continuous readout, the positions are adjusted for each gap between SiPM chips, SiPM arrays, and PCBs.

As a result, the discontinuity previously observed in panel a) is completely removed, demonstrating the effectiveness of the applied correction. The global tilt of the distribution remains unchanged, as it originates from the geometrical configuration of the experiment and not from the readout structure. Compared to panel a), Δx is shifted to slightly larger values, reflecting the increased effective detector length introduced by the inclusion of the gap sizes in the position reconstruction.

The result of the analysis presented so far is the determination of the cluster positions independently for the bottom and top sides of Fib70, which are expected to be correlated for a single particle traversing the detector. Figure 9 shows the spatial correlation of events recorded on the top and bottom sides for a small fraction of Fib70. The top panel shows the correlation obtained using the fit method. The correlation appears as a narrow band with a large number of localized clusters close to the x=y diagonal. The small shift by 0.6 mm with respect to the x=y diagonal is due to a slight misalignment between the SiPMs on the top and bottom of the detector. This reflects the precision achievable in the manufacturing and assembly process. The lower panel shows the same correlation for the CoG method. Here, the same structure is again visible but broader than in the fit method, reflecting the poorer position resolution.

The origin of the localized clusters is related to the granularity of the fiber ribbon. The centroids of the individual localized clusters in this correlation matrix were determined and the distances between neighboring clusters were calculated. The resulting distribution is shown in Fig. 10, where an average value of 188(16) μm is obtained. This is in good

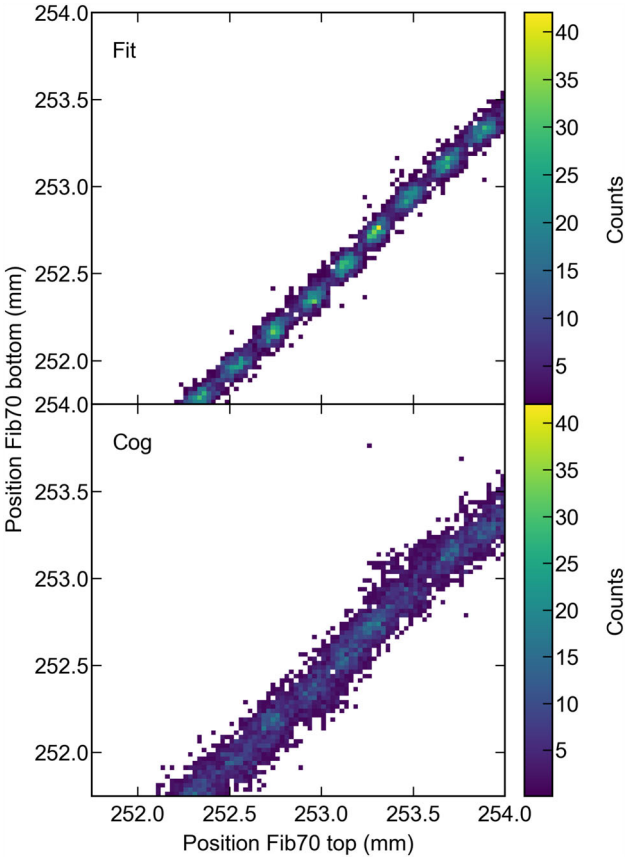


Fig. 9 Position correlation between the top and bottom sides of the Fib70 detector for the fit method (top) and CoG method (bottom). The nearly diagonal structure corresponds to correlated hits from single ions, while the localized clusters reflect the granularity of the scintillating fiber ribbon

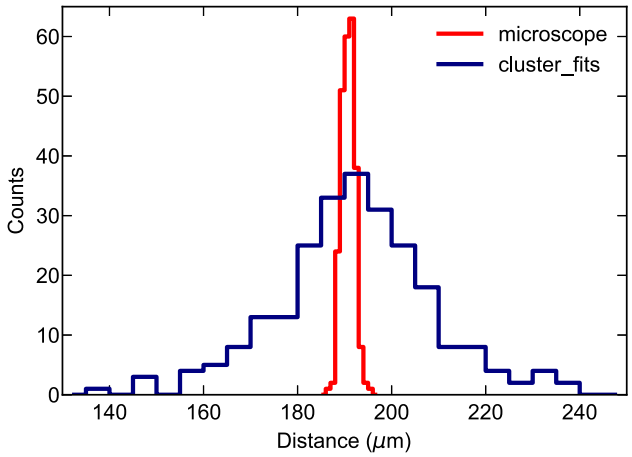


Fig. 10 Distribution of distances between neighboring localized clusters in the top–bottom correlation matrix. The mean value reflects the effective spacing of individual scintillating fibers in the ribbon

agreement with the average width of the scintillating fibers in the ribbon, measured with a microscope after the winding process, which yielded a value of 190.8(16) μm. This value is slightly smaller than the nominal fiber width of 200(6) μm specified by Kuraray.

This result confirms that the localized clusters observed in Fig. 9 correspond to individual scintillating fibers. It demonstrates that individual fibers can be resolved, even though the SiPM channel width exceeds the fiber width, highlighting the capability of the detector to achieve fiber-level spatial resolution.

6.2 Results

The analysis described in the previous section provides the reconstructed hit positions of particles independently for the top and bottom sides of the Fib70 detector. These position measurements can either be used separately for each detector side or combined by requiring a coincidence between both sides. The latter provides a more unambiguous identification of particle hits, while the former can offer a higher detection efficiency. In the following, both approaches are investigated.

By reconstructing the positions at which the ions interact with the detector, it is possible to inspect the profile of the incoming ^{107}Ag beam. Figure 11 shows the beam profiles obtained using the fit method in the left column, while the profiles reconstructed with the CoG method are shown in the right column. The first and second rows display the results for the top and bottom sides of the detector, respectively. The histograms in the bottom row only include events that were detected simultaneously on both sides of the detector. These events must be separated by no more than 1 mm to ensure that the recorded signals originate from the same ion that passed through the detector. These conditions are fulfilled for about 97% of the total recorded events.

In all shown histograms, the beam profile exhibits an approximately Gaussian shape, as expected for an unreacted beam at R^{3}B. Pronounced dips are visible at a position of 262 mm, which corresponds to the location of the gap between the second and third PCBs of the SiPM readout.

Since the SiPM readout of the top and bottom sides of the detector is symmetric, the dips appear at approximately the same positions in both cases. As discussed in Sect. 6.1, the scintillation light produced by fibers located within or close to such a gap is only partially detected by the SiPMs. As a result, the measured ToT distribution is affected, in particular when the maximum of the light distribution is not fully recorded. Such events may either be lost due to an unsuccessful position reconstruction or result in a reconstructed position shifted towards the edge of the gap.

This effect is particularly pronounced when using the CoG method for position reconstruction, as it does not compensate for incomplete ToT distributions. This leads to the appear-

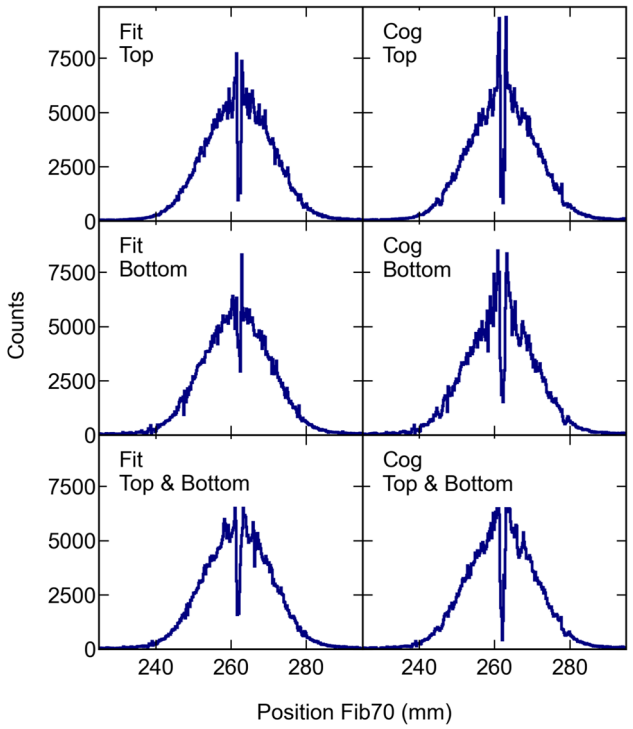


Fig. 11 Beam profiles obtained by reconstructing the ion hit positions with the fit (left) and CoG (right) methods. The top and middle rows show the results from the top and the bottom side of the Fib70 detector, respectively. The bottom row shows events that were simultaneously detected at both detector sides

ance of spikes adjacent to the dips, which are more pronounced for the CoG method than for the fit method.

6.2.1 Efficiency

The detection efficiency is one of the key performance parameters of the Fib70 detector. Its determination requires an external reference detector that provides an independent and reliable measurement of particle hits. For this purpose, the Fib41 detector is used, which, as discussed above, allows for an unambiguous position determination without the need for further corrections. In addition, the correlation between the positions measured in Fib41 and Fib70 enables the determination of the Fib70 efficiency as a function of position along the x-axis.

The spatial correlation between events recorded in both detectors is shown in Fig. 12, where only events detected simultaneously on the top and bottom sides of Fib70 are included. The figure shows that events recorded in both detectors are clearly correlated, resulting in the beam spot appearing as a confined diagonal line. Only a small number of events are not associated with the beam spot, demonstrating that random coincidences between the Fib70 and Fib41 detectors are negligible. Those events could also be scattered events or reactions in the first fiber detector.

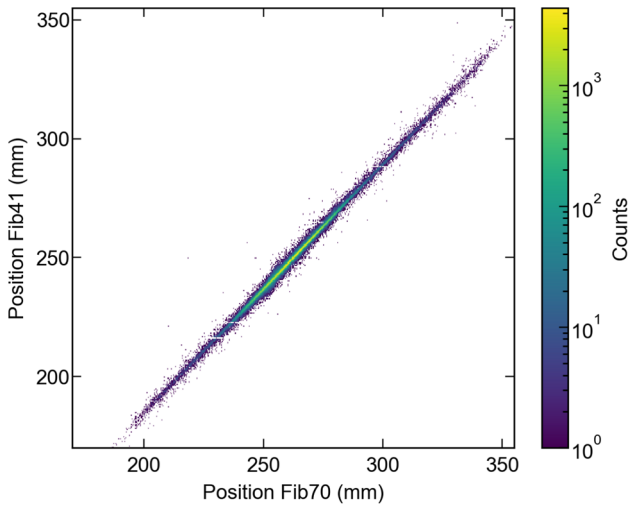


Fig. 12 Position correlation of the Fib70 detector and the Fib41 reference detector

The relative efficiency for detecting heavy ions in the Fib70 detector is defined as

$$\epsilon_{\text{Fib70}} = \frac{\sum \text{Events in Fib70 \& Fib41}}{\sum \text{Events in Fib41}}. \tag{4}$$

The uncertainty is calculated using the 95% Wilson confidence interval, assuming an underlying binomial distribution. Figure 13 presents the relative efficiencies for the top side, bottom side, and for events detected simultaneously on both sides of the Fib70 detector. The efficiencies are shown as a function of position along the Fib70 detector. For this purpose, the positions determined in Fib41 are mapped onto the Fib70 coordinate system using the measured correlation between both detectors. Results for the fit and CoG reconstruction methods are shown separately. With both position reconstruction methods, a high efficiency of approx. 97% is achieved (average of all data points using the fitting method and requiring top and bottom side) Fig. 13.

The gaps in the SiPM readout also affect the efficiency of the Fib70 detector. This is the cause of the sudden drop in efficiency at a position of 262 mm, which corresponds, as before, to the gap between two PCBs. When using the fit method for position reconstruction, the efficiency drops to a minimum of 57% for the top detector and 88% for the bottom detector at the position of the gap. Correlating the top and bottom sides results in an efficiency of 54%, which is mainly determined by the less efficient detector side. Excluding the gap positions in the calculation of the average efficieny results in 97.8%, which is only slightly larger compared to the overall average efficiency due to the small sizes of the gaps.

With the CoG method, the efficiencies of the top and bottom detectors remain nearly constant across the detector area. However, when correlating hits from the top and bottom

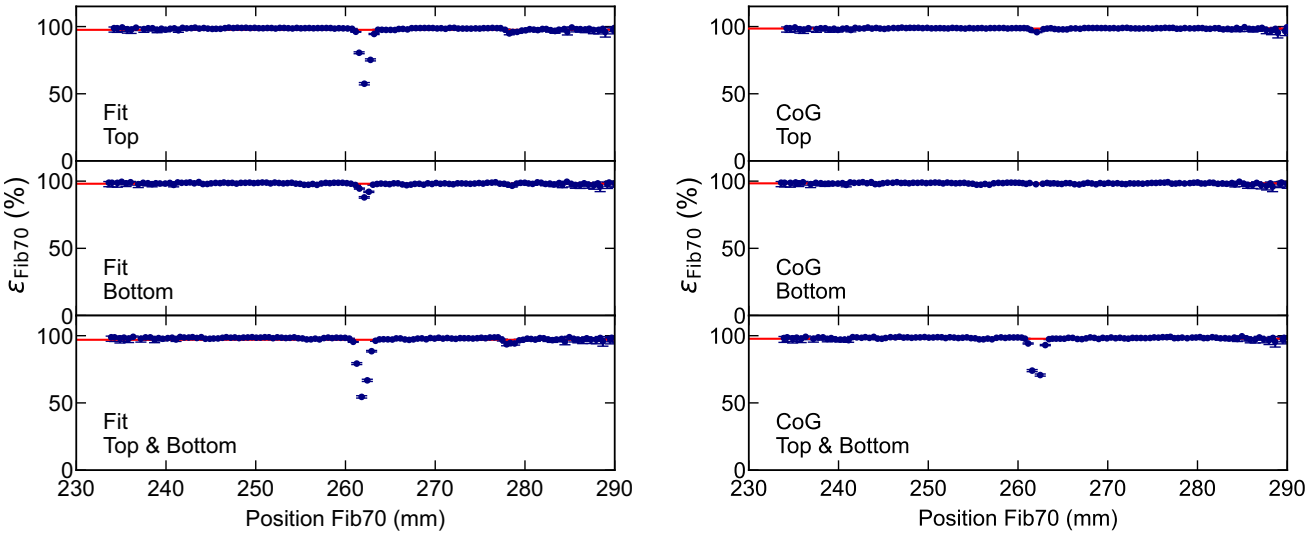


Fig. 13 Efficiency of the Fib70 detector relative to the reference detector Fib41 obtained by reconstructing the event position by the fit method (left) and CoG method (right). Efficiencies are shown for the top (top) and bottom (middle) sides of Fib70 separately, as well as for events recorded simultaneously at both sides. The red horizontal lines indicate the average efficiency of each panel, which is approx. 97% for all considered cases

sides, the efficiency drops to 70%. While the CoG method can, in principle, reconstruct events affected by gaps, it tends to shift their positions if the distribution of scintillation light is not fully recorded. As a result, the spatial correlation between the top and bottom sides can be lost, as they appear to have occurred at different positions, suggesting they do not belong to the same ion.

These results indicate that both the fiber ribbon and the SiPM readout have a high intrinsic efficiency, as nearly every ion recorded in Fib41 produces sufficient scintillation light in Fib70 to be detected. The observed inefficiency is therefore mainly attributed to limitations of the position reconstruction, particularly in cases where the scintillation light distribution is only partially recorded.

6.2.2 Resolution

The spatial resolution is, alongside the detection efficiency, one of the key performance parameters of the Fib70 detector. Ideally, the resolution would be determined using an external reference detector with superior spatial resolution. However, the Fib41 detector does not fulfill this requirement, and Fib70 currently represents the tracking detector with the highest spatial resolution available at R^3B. Therefore, the resolution has to be determined intrinsically.

As discussed in the previous section, the correlation between the reconstructed cluster positions on the top and bottom sides of the detector exhibits a discrete structure corresponding to individual scintillating fibers. This already indicates that the achievable resolution is on the order of the fiber width. A quantitative estimate can be obtained by treating the top and bottom sides of Fib70 as independent position measurements.

The position difference $\Delta x = x_{\mathrm{top}} - x_{\mathrm{bottom}}$ is calculated for events detected simultaneously on both sides of the detector. The spread of Δx provides a measure of the position resolution, as it reflects how precisely the origin of the scintillation light–and thus the hit fiber–can be determined. Figure 14 shows the position difference Δx as a function of the event position in the Fib70 bottom detector, where the positions were reconstructed using the fit method. The right panel of the figure shows the projection of Δx from the region within the red dashed lines onto the y-axis, along with a Gaussian fit. The standard deviation of this Gaussian is taken as a measure of the position resolution at the selected detector position.

The broadening observed at 262 mm indicates a degradation of the position resolution at the gap between the PCBs, as discussed in the previous sections. Averaging over the full detector area yields a standard deviation of 68.0(6) μm for the difference spectra when using the fit method for position reconstruction, compared to 97(2) μm for the CoG method. These values therefore represent the combined error of both sides.

This result demonstrates that the achieved resolution is sufficient to identify the fiber in which the scintillation light was produced. In particular, the resolution of about 70 μm obtained from the comparison of the top and bottom detector

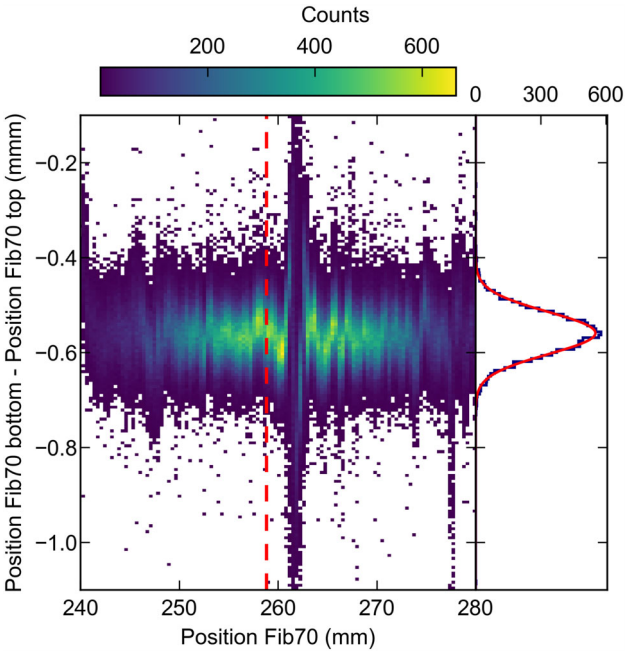


Fig. 14 Position difference $\Delta x = x_{\text{top}} - x_{\text{bottom}}$ as a function of the reconstructed position in the Fib70 bottom detector (left). The right panel shows the projection of Δx at the position indicated by the dashed lines, together with a Gaussian fit used to extract the position resolution

sides confirms that the Fib70 detector is capable of reaching the intrinsic spatial resolution defined by the granularity of the scintillating fiber ribbon.

7 Summary

A new large-area scintillating fiber tracking detector for heavy-ion measurements at the R^3B setup has been developed and commissioned. The detector is based on a single-layer ribbon of square scintillating fibers with a cross section of 0.2 mm × 0.2 mm and SiPM array readout at both fiber ends. Its design is optimized for operation in the magnetic-field environment of the R^3B setup while providing a low and homogeneous material budget, which is essential for minimizing energy-loss and angular straggling of relativistic heavy ions.

The production of the scintillating fiber ribbon was established using a dedicated winding procedure that yields a homogeneous, gap-free ribbon structure over large areas. Optical quality control confirmed the high geometrical quality of the produced ribbon and showed that the fiber dimensions are consistent with the manufacturer specifications. The mechanical design of the detector provides the required active area, sufficient rigidity for stable operation, and the integration of the cooling and readout systems under vacuum conditions.

The detector performance was investigated in a beam test behind the GLAD magnet at the R^3B setup using a ^{107}Ag beam at 1 GeV/u. A dedicated analysis procedure was developed to reconstruct the ion hit positions from the time-over-threshold distributions measured in the SiPM channels. Both, a center-of-gravity method and a Gaussian fit approach were studied. The results show that the detector is capable of resolving individual scintillating fibers, despite the SiPM channel pitch being larger than the fiber width.

Using the Fib41 detector as an external reference, the relative efficiency of Fib70 was determined as a function of position. Average efficiencies of 97% or higher were obtained for both reconstruction methods. The remaining local inefficiencies are mainly related to the reconstruction of events affected by gaps in the SiPM readout structure rather than to a limited intrinsic detection efficiency of the scintillating fibers or the photosensors.

The spatial resolution was estimated intrinsically by comparing the reconstructed positions on the top and bottom detector sides. A resolution of 68.0(6) μm was obtained with the fit method, compared to 97(2) μm for the center-of-gravity method. These results demonstrate that the detector reaches a spatial resolution at the level of the fiber granularity and is able to identify the fiber in which the scintillation light was produced.

Overall, the presented detector fulfills the main requirements for its application as a tracking detector for relativistic heavy ions at R^3B. In particular, it combines high efficiency, fiber-level spatial resolution, large active area, and compatibility with operation close to magnetic fields, making it a suitable detector concept for future heavy-ion experiments at FAIR.

Acknowledgements We would like to acknowledge the assistance of Blake Leverington in giving invaluable insights, guidance, and fruitful discussions throughout this research.

Funding Open Access funding enabled and organized by Projekt DEAL. P. Garcia Gil and E. Casarejos have been partially funded by MICIU/AEI/10.13039/501100011033/ (PID2021-125771NB-C22, PID2024-157431NB-C22). The project is receiving funding from NRW-FAIR within the programme "Netzwerke 2021", an initiative of the Ministry of Culture and Science of the State of Northrhine Westphalia. This work has been supported by the GSI-TU Darmstadt Cooperation Agreement. The results presented here are based on data taken during a GSI Directors beam time, which was performed at the beam line HTC at the GSI Helmholtzzentrum fuer Schwerionenforschung, Darmstadt (Germany) in the frame of FAIR Phase-0'. The publication is funded by the Open Access Publishing Fund of GSI Helmholtzzentrum fuer Schwerionenforschung.

Data availability statement Data will be made available on reasonable request. [Authors' comment: The datasets generated during and/or analysed during the current study are available from the corresponding author on reasonable request.].

Code availability statement Code/software will be made available on reasonable request. [Authors' comment: The code/software generated during and/or analysed during the current study is available from the corresponding author on reasonable request.].

Open Access This article is licensed under a Creative Commons Attribution 4.0 International License, which permits use, sharing, adaptation, distribution and reproduction in any medium or format, as long as you give appropriate credit to the original author(s) and the source, provide a link to the Creative Commons licence, and indicate if changes were made. The images or other third party material in this article are included in the article's Creative Commons licence, unless indicated otherwise in a credit line to the material. If material is not included in the article's Creative Commons licence and your intended use is not permitted by statutory regulation or exceeds the permitted use, you will need to obtain permission directly from the copyright holder. To view a copy of this licence, visit http://creativecommons.org/licenses/by/4.0/.

References

1. S. Reimann, H. Albers, R. W. Assmann1, P. Gasik, O. Geithner, F. Hagenbuck, A. Herlert andP. Hofmann, V. Kamerdzhiev, M. Kauschke, H. Kollmus, S. Pietri, N. Pyka, T. Radon, C. Schroeder, S. Schwarz, H. Simon, P. Spiller, K. Vogt, Fair commissioning - towards first science. In: Proc. 16th International Particle Accelerator Conference, number 16 in IPAC'25 - 16th International Particle Accelerator Conference, pages 2495–2498. JACoW Publishing, Geneva, Switzerland, 06 (2025)
2. T Aumann, C A Bertulani, M Duer, T Galatyuk, A Obertelli, V Panin, J L Rodríguez-Sánchez, R Roth, and J Stroth. Nuclear structure opportunities with gev radioactive beams at fair. Philos. Trans. R. Soc. A: Math. Phys. Eng. Sci. **382**, 20230121, 6 (2024)
3. W.R. Leo, *Techniques for Nuclear and Particle Physics Experiments* (Springer, New York, 1994)
4. C. Trippl, G. Haefeli, O. Schneider, E. Zaffaroni, Microlens-enhanced silicon photomultiplier arrays for lhcb scifi tracker upgrade ib. Nucl. Instrum. Methods Phys. Res., Sect. A **1040**, 10 (2022)
5. Lukas Gruber. Lhcb scifi – upgrading lhcb with a scintillating fibre tracker. Nuclear Instruments and Methods in Physics Research Section A: Accelerators, Spectrometers, Detectors and Associated Equipment, 958:162025, 2020. Proceedings of the Vienna Conference on Instrumentation (2019)
6. A. Massafferri, Scifi, the new tracker of the lhcb experiment. J. Instrum. **15**(08), C08006 (2020)
7. A. Bravar, K. Briggl, S. Corrodi, A. Damyanova, L. Gerritzen, C. Grab, M. Hildebrandt, A. Papa, G. Rutar, The mu3e scintillating fiber timing detector. Nucl. Instrum. Methods Phys. Res., Sect. A **958**, 4 (2020)
8. D. Renker, E. Lorenz, Advances in solid state photon detectors. J. Instrum. **4**, P04004 (2009)
9. M. Heil, A. Kelić-Heil, L. Bott, et al. A new time-of-flight detector for the r3b setup. Eur. Phys. J. A **58:12**, 1–19 (2022)
10. Kuraray. Kuraray - plastic scintillating fibers. http://kuraraypsf.jp/pdf/all.pdf. Accessed: 2026-03-30
11. LHCb Collaboration. The lhcb upgrade i. Journal of Instrumentation, 19(5), Cited by: 43 (All Open Access, Green Open Access, Hybrid Gold Open Access, 2024)
12. Hamamatsu. Mppc array s13552 | hamamatsu photonics. https://www.hamamatsu.com/eu/en/product/optical-sensors/mppc/mppc_mppc-array/S13552.html. Accessed: 30 March 2026
13. GSI-FAIR. Gsi-fair scientific report (2022)
14. R3B-Collaboration. Nustar tdr - r3b - glad (2011)